Model Predictive Control of the Vertical Gradient Freeze Crystal Growth Process

Stefan Ecklebe [*] **Tom Buchwald** [**] **Patrick Rüdiger** [***]
Jan Winkler [*]

[*] *Institute of Control Theory, Technische Universität Dresden, 01062 Dresden, Germany (email: {stefan.ecklebe, jan.winkler}@tu-dresden.de)*
[**] *Institute of Traffic Engineering, Brandenburg University of Technology Cottbus-Senftenberg, 03046 Cottbus, Germany (email: tom.buchwald@b-tu.de)*
[***] *Institute of Natural Materials Technology, Technische Universität Dresden, 01062 Dresden, Germany (email: patrick.ruediger@tu-dresden.de)*

Abstract: This contribution presents the application of nonlinear model predictive control to the Vertical Gradient Freeze crystal growth process. Due to the time-varying spatial extent of the crystal and melt during growth, this process is characterised by two coupled free boundary problems that form a so called two-phase Stefan problem which is of nonlinear nature. To apply model predictive control to this process, a simplified, spatially distributed representation of the system is derived and transferred into a spatially lumped form by means of the finite element method. For this model, a nonlinear control problem is formulated, that takes process limitations into account and tries to satisfy different quality objectives by formulating demands on the systems spatiotemproal temperature distribution. This provides the foundation for the presented predictive control design. Finally, the approximated model and the controller are verified for different real-world scenarios that include model errors and parameter uncertainties.

Keywords: Vertical Gradient Freeze, Two-phase Stefan problem, Distributed parameter systems, Free boundary value problem, Nonlinear control systems, Predictive control

1. INTRODUCTION

1.1 Motivation

Unlike the more common Czochralski (CZ) process (Friedrich et al., 2015) in which crystals are grown from the melt in an upside-down configuration, the Vertical Gradient Freeze (VGF) technique uses an upward growth direction which is more beneficial in terms of the heat flow in the crystal. Therefore, it can be used for the bulk production of high quality compound semiconductor single crystals (Jurisch et al., 2005) like Gallium-Arsenide (GaAs) or Indium-Phosphide that are hard to grow in a CZ setup.

In detail, the process sketched in Figure 1 works as follows: A seed crystal is placed at the bottom of a rotationally symmetric crucible which is later filled with solid semiconductor chunks. After all material (up to the seed) in the crucible is molten, a vertical temperature gradient is moved through the plant such that a single crystal grows from the bottom to the top. While doing so, the crystallisation interface must be kept in a flat or slightly convex shape to avoid the creation of stacking faults whose occurrence can lead from degraded properties up to twinning and thus unusable crystals. Typically, the process inputs are the heat flows into the system, applied
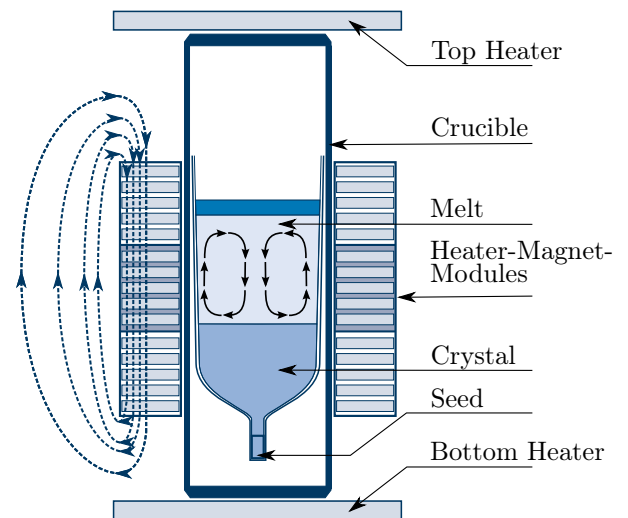

Fig. 1. Sketch of a VGF crystal growth furnace and associated magnet and flow fields.

by the the heaters surrounding the crucible. However, in a CGD Kronos[©] plant (Frank-Rotsch et al., 2014), the three jacket heaters are also designed as Heater-Magnet-Modules, allowing to apply a magnetic field that can drive a flow field which in turn increases heat transport by means of forced convection.

The underlying physical process can be described by two free boundary problems (FBPs) for crystal and melt, coupled by the dynamics of the crystal-melt interface that form a nonlinear two-phase Stefan problem (TPSP) (Crank, 1984). This interesting type of system is already broadly discussed in the framework of distributed parameter systems (DPSs) with works including Lyapunov-based (Petrus et al., 2010), flatness-based (Ecklebe et al., 2021), backstepping-based (Koga et al., 2019), (Ecklebe et al., 2020) and optimal (Kang and Zabaras, 1995; Hinze et al., 2009) control designs. However, at this point, no designs are available that adhere to the plant limitations as there are for the CZ process (Abdollahi et al., 2014; Rahmanpour et al., 2016), or that incorporate the melt convection as degree of freedom. This motivates the present work.

1.2 Objective & structure

The main objective of this contribution is to present a nonlinear model predictive control (NMPC) design for the VGF growth process. To do so, Section 2 derives a simplified one-dimensional distributed parameter model of the process that contains the most important effects. Next, this model is approximated by using the finite element method (FEM) in Section 3. Based on this system, the main Section 4 formulates a nonlinear control problem that expresses the system limitations and process requirements and describes the complete control setup. Afterwards, the result Section 5 discusses the verification of the FEM model, the control performance as well as the effects of parameter uncertainties and disturbances. Finally, a summary and an outlook to further work is given.

2. INFINITE DIMENSIONAL MODEL

As the foundation for model based control, this section introduces a reduced one dimensional distributed parameter model based on the real VGF process plant.

2.1 Two-dimensional model

In both crystal and melt, the quantity under consideration is given by the scalar temperature field $\vartheta(\boldsymbol{p}, t)$ at the position vector $\boldsymbol{p}$ and time t. In contrast to the diffusive-only energy transport in the solid crystal, the liquid melt also enables convective heat transport. However, due to the small Prandtl numbers of the materials (e.g. GaAs with 0.068) that denote the ratio of convective to diffusive heat transport, the natural convection can be neglected and only the forced convection $\boldsymbol{v}(\boldsymbol{p}, t)$ through the application of external magnetic fields is modelled. Now, by assuming piecewise constant physical properties for the solid and the liquid phase with the density ρ, the specific heat capacity c_{p}, and thermal conductivity λ, the governing equation for each phase reads:

$$\rho c_{\mathrm{p}} \partial_t \vartheta(\boldsymbol{p}, t) = \lambda \Delta \vartheta(\boldsymbol{p}, t) - c_{\mathrm{p}} \rho \boldsymbol{v}(\boldsymbol{p}, t) \nabla \vartheta(\boldsymbol{p}, t). \quad (1)$$

Herein, the partial derivative of $\vartheta(\boldsymbol{p}, t)$ w.r.t. $\circ$ is given by $\partial_\circ \vartheta(\boldsymbol{p}, t)$, just as the Laplacian and gradient of $\vartheta(\boldsymbol{p}, t)$ are denoted as $\Delta \vartheta(\boldsymbol{p}, t)$ and $\nabla \vartheta(\boldsymbol{p}, t)$, respectively. As the equations for crystal and melt are similar, in the following only one generic expression is stated, which can be specified for the solid or liquid part by using the indices "s" and
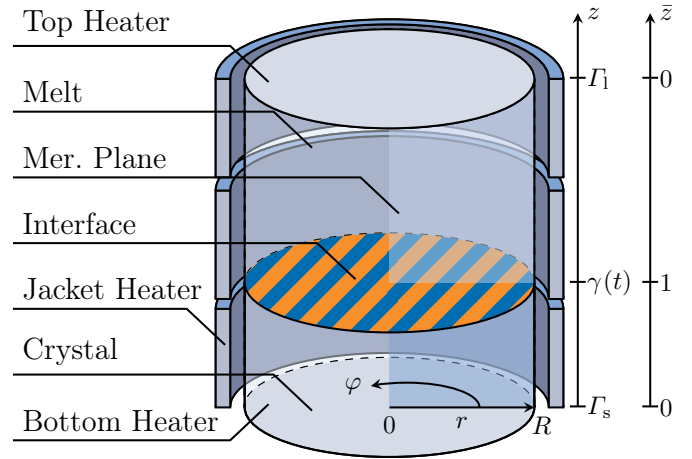

Fig. 2. Simplified plant model with cylindrical coordinates $\boldsymbol{p} = (r, \varphi, z)$ and the scaled coordinate frame $\bar{z}$.

"l", respectively. For example, there is no convection in the crystal and thus, $\boldsymbol{v}_{\mathrm{s}}(\boldsymbol{p}, t) = 0$.

Due to the geometry of the crucible, (1) is localised in cylindrical coordinates with radius r, angle φ as well as height z as shown in Figure 2. Since the plant is rotationally symmetric, the dependency on φ can be dropped which reduces the problem to the 2d temperature distributions in the meridional rz-planes of the crystal and the melt, each reaching from its system boundary Γ to the moving interface $\gamma(r, t)$:

$$\begin{aligned}
\partial_t \vartheta(r, z, t) = {}& \alpha \left(\tfrac{1}{r} \partial_r \left(r \partial_r \vartheta(r, z, t) \right) + \partial_z^2 \vartheta(r, z, t) \right) \\
& - v_r(r, z, t) \partial_r \vartheta(r, z, t) \\
& - v_z(r, z, t) \partial_z \vartheta(r, z, t)
\end{aligned} \quad (2)$$

for $z \in (\Gamma, \gamma(r, t))$, $r \in (0, R)$ and $t \in \mathbb{R}^+$. Herein, $\alpha := \lambda / (\rho c_{\mathrm{p}})$ denotes the thermal diffusivity and $v_r(r, z, t)$ and $v_z(r, z, t)$ represent the remaining components of $\boldsymbol{v}(r, z, t)$.

Due to the ongoing phase transition, the temperature at the interface $\vartheta(r, \gamma(r, t), t)$ is fixed at the melting point temperature T_{m}. Furthermore, due to the rotational symmetry, the radial heat flow at $r = 0$ is always zero. Thus, by denoting the top/bottom and jacket heat flows as $q(r, t)$ and $q_{\mathrm{m}}(z, t)$, the boundary conditions of (2) read:

$$\lambda \partial_z \vartheta(r, \Gamma, t) = \delta q(r, t) \quad (3a)$$
$$\lambda \partial_r \vartheta(R, z, t) = q_{\mathrm{m}}(z, t) \quad (3b)$$
$$\partial_r \vartheta(0, z, t) = 0 \quad (3c)$$
$$\vartheta(r, \gamma(r, t), t) = T_{\mathrm{m}} \quad (3d)$$

with the orientation factor δ taking the value of -1 in the crystal and 1 in the melt. Herein, $q_{\mathrm{m}}(z, t)$ describes an arbitrary lateral heat flow profile, in practice however, only three distinct heaters exist. Therefore, $q_{\mathrm{m}}(z, t)$ is given by

$$q_{\mathrm{m}}(z, t) = \sum_{i=1}^{3} \psi_i(z) u_{\mathrm{m}, i}(t) = \boldsymbol{\psi}(z) \boldsymbol{u}_{\mathrm{m}}(t) \quad (4)$$

with the intensity profiles $\psi_i(z) := b_i z^2 + c_i z + d_i$, deduced from the plant geometry and experiments and condensed in $\boldsymbol{\psi}(z) := (\psi_1(z) \ \psi_2(z) \ \psi_3(z))$. Furthermore, the actual jacket heat flows are denoted by $u_{\mathrm{m}, i}(t)$ with their corresponding vector $\boldsymbol{u}_{\mathrm{m}}(t)^T := (u_{\mathrm{m}, 1}(t) \ u_{\mathrm{m}, 2}(t) \ u_{\mathrm{m}, 3}(t))$.

2.2 One-dimensional model

For the control design it is assumed that the heat loss in radial direction can be neglected. This enables averaging over the radius and reducing the spatial domain to a line with the new temperature defined as:

$$T(z,t) := \frac{2}{R^2} \int_0^R \vartheta(r,z,t) r \, dr . \tag{5}$$

Furthermore, assume that the radial component of the forced convection field has zero mean such that $\int_0^R v_r(r,z,t) \, dr = 0$. Lastly, assume that $v_z(r,z,t)$ can be written as $v_z(r,z,t) = \chi_v(r,z)\bar{u}_v(t)$ with a fixed vortex-characteristic $\chi_v(r,z)$ and scaling $\bar{u}_v(t)$, realised by the heater-magnet-modules. Thus, integration of (2) over r and scaling by R^{-2} yields the final FBP

$$\partial_t T(z,t) = \alpha \partial_z^2 T(z,t) - \psi_v(z)\bar{u}_v(t)\partial_z T(z,t) + \boldsymbol{\psi}(z)\bar{\boldsymbol{u}}_m(t) \tag{6a}$$

$$\lambda \partial_z T(\Gamma,t) = \delta u(t) \tag{6b}$$

$$T(\gamma(t),t) = T_m \tag{6c}$$

where $\psi_v(z) := \frac{1}{R}\int_0^R \chi_v(r,z) \, dr$ and $u(t) := \frac{1}{R}\int_0^R q(r,t) \, dr$ represent the radially averaged vortex characteristic and heat flow, respectively. Furthermore, $\bar{\boldsymbol{u}}_m(t) := \boldsymbol{u}_m(t) \, 2/(R\rho c_p)$ denotes the scaled former boundary (3b) that now acts as in-domain actuation.

Next, examining the energy balance at the reduced interface $\gamma(t)$ yields the Stefan condition (Stefan, 1891)

$$\rho_m L \dot{\gamma}(t) = \lambda_s \partial_z T_s(\gamma(t),t) - \lambda_l \partial_z T_l(\gamma(t),t) \tag{7}$$

which describes the evolution of the phase boundary. Herein, ρ_m denotes the density of the melt at melting temperature and L the specific latent heat.

3. FINITE DIMENSIONAL APPROXIMATION

Although the spatially distributed model's equations are quite elegant in terms of notation, to apply the standard methods for NMPC, a spatially lumped model is needed. Therefore, this section introduces a lumped nonlinear state space system of the form

$$\dot{\boldsymbol{x}}(t) = f(\boldsymbol{x}(t), \boldsymbol{u}(t)) \tag{8}$$

with the initial state $\boldsymbol{x}(0) = \boldsymbol{x}^0$ using the FEM.

3.1 Series expansion

To obtain a finite dimensional approximation, the temperature distribution $T(z,t)$ in each of the two phases is approximated by a test solution of order N

$$T^N(z,t) := \sum_{i=1}^N \varphi_i^N(z) w_i^N(t), \tag{9}$$

formed by the spatial *shape functions* $\varphi_i^N(z)$ and the time dependent *weights* $w_i^N(t)$.

Note that this separation ansatz leaves no option for the shape functions $\varphi_i^N(z)$ to depend on the time t. Since the growing crystal and the decrease of melt will alter the spatial domain for both phases over time it is required to introduce a coordinate transformation in such a way that the spatial domain in the transformed system remains constant over the process. This can be realized by writing

the system in new coordinates using a slightly modified version of the boundary immobilisation method as used in (Wouwer et al., 2001; Maidi and Corriou, 2014):

$$\bar{T}(\bar{z},t) := T(z,t) \quad \bar{z} := \frac{z-\Gamma}{\beta(t)} \quad \beta(t) := \gamma(t) - \Gamma, \tag{10}$$

whose spatial domain $\bar{z} \in (0,1)$ is shown on the right-hand side of Figure 2. Note that this mapping is only well-defined as long as there is a crystal and a melt, thus $\gamma(t) \neq \Gamma$. However, since the process is started with a seed crystal this does not pose a problem in the beginning and once the melt is solidified the problem reduces to a single heat equation with constant domain, rendering it even simpler in the end.

Thus, the two resulting fixed systems coupled via $\dot{\gamma}(t)$ which is in turn given by the transformed variant of the Stefan condition (7) are obtained after short computation [1]:

$$\partial_t \bar{T}(\bar{z},t) = a_2(t)\partial_{\bar{z}}^2 \bar{T}(\bar{z},t) + a_1(\bar{z},t)\partial_{\bar{z}} \bar{T}(\bar{z},t) + \bar{\boldsymbol{\psi}}(\bar{z},t)\bar{\boldsymbol{u}}_m(t) \tag{11a}$$

$$\partial_{\bar{z}} \bar{T}(0,t) = \bar{u}(t) \tag{11b}$$

$$\bar{T}(1,t) = T_m \tag{11c}$$

$$\dot{\gamma}(t) = s_s(t)\partial_{\bar{z}} \bar{T}_s(1,t) + s_l(t)\partial_{\bar{z}} \bar{T}_l(1,t). \tag{11d}$$

Amongst other things, the substitutions $a_2(t) := \alpha/\beta^2(t)$ and $a_1(\bar{z},t) := \left(\bar{z}\dot{\gamma}(t) - \bar{\psi}_v(\bar{z})\bar{u}_v(t)\right)/\beta(t)$ were made.

Now, the approximation of the series expansion (9) can be expressed in the transformed coordinates

$$\bar{T}^N(\bar{z},t) = \sum_{i=1}^N \bar{\varphi}_i^N(\bar{z})\bar{w}_i^N(t) \tag{12}$$

with the shape functions $\bar{\varphi}_i^N(\bar{z})$, $i = 1,\ldots,N$. Note that herein only one set of shape functions is utilised for both phases due to their consistent domains. For the approximation, piecewise-linear Lagrangian (aka "hat") functions with the spatial discretisation $\delta_{\bar{z}} := \frac{1}{N-1}$, are used. In detail, they are given by

$$\bar{\varphi}_i^N(\bar{z}) := \begin{cases} \frac{\bar{z}-(i-2)\delta_{\bar{z}}}{\delta_{\bar{z}}} & \text{for } (i-2)\delta_{\bar{z}} < \bar{z} \le (i-1)\delta_{\bar{z}} \\ \frac{i\delta_{\bar{z}}-\bar{z}}{\delta_{\bar{z}}} & \text{for } (i-1)\delta_{\bar{z}} < \bar{z} < i\delta_{\bar{z}} \\ 0 & \text{otherwise} \end{cases} \tag{13a}$$

for the general case $i \notin \{1,N\}$ and

$$\bar{\varphi}_1^N(\bar{z}) := \begin{cases} \frac{\delta_{\bar{z}}-\bar{z}}{\delta_{\bar{z}}} & \text{for } 0 < \bar{z} < \delta_{\bar{z}} \\ 0 & \text{otherwise} \end{cases} \tag{13b}$$

as well as

$$\bar{\varphi}_N^N(\bar{z}) := \begin{cases} \frac{\bar{z}-(N-2)\delta_{\bar{z}}}{\delta_{\bar{z}}} & \text{for } (N-2)\delta_{\bar{z}} < \bar{z} \le 1 \\ 0 & \text{otherwise} \end{cases} \tag{13c}$$

at the outer and inner boundary, respectively.

Hence, the Dirichlet boundary condition (11c) directly evaluates to $\bar{w}_N^N(t) = T_m$, since only $\bar{\varphi}_N^N(\bar{z})$ differs from zero at $\bar{z} = 1$. Thus, by introducing the vector of the remaining free variables $\bar{\boldsymbol{w}}^N(t)^T := \left(\bar{w}_1^N(t) \cdots \bar{w}_{N-1}^N(t)\right)$ and the shape function vector $\bar{\boldsymbol{\varphi}}^N(\bar{z}) := \left(\bar{\varphi}_1^N(\bar{z}) \cdots \bar{\varphi}_{N-1}^N(\bar{z})\right)$, the approximation (12) can be given by

$$\bar{T}^N(\bar{z},t) = \bar{\boldsymbol{\varphi}}^N(\bar{z})\bar{\boldsymbol{w}}^N(t) + \bar{\varphi}_N^N(\bar{z})T_m. \tag{14}$$

---

[1] Please refer to Appendix A for details.

3.2 Projection

Using the Galerkin method, (11a) is projected on the functions from $\bar{\boldsymbol{\varphi}}^N(\bar{z})$, yielding equations of the form

$$\langle \partial_t \bar{T}^N(\bar{z},t)|\bar{\varphi}_k^N(\bar{z})\rangle = a_2(t)\langle \partial_{\bar{z}}^2 \bar{T}^N(\bar{z},t)|\bar{\varphi}_k^N(\bar{z})\rangle$$
$$+ \langle a_1(\bar{z},t)\partial_{\bar{z}}\bar{T}^N(\bar{z},t)|\bar{\varphi}_k^N(\bar{z})\rangle \quad (15)$$
$$+ \langle \bar{\boldsymbol{\psi}}(\bar{z},t)|\bar{\varphi}_k^N(\bar{z})\rangle \bar{\boldsymbol{u}}_{\mathrm{m}}(t)$$

for $k = 1, \ldots, N-1$. Herein, $\langle a(\xi)|b(\xi)\rangle = \int_0^1 a(\xi)b(\xi)\,\mathrm{d}\xi$ denotes the standard inner product on L_2 for real-valued arguments. Performing integration by parts on the second order term of (15) gives the weak form of the problem:

$$\langle \partial_t \bar{T}^N(\bar{z},t)|\bar{\varphi}_k^N(\bar{z})\rangle = a_2(t)\Big(\big[\partial_{\bar{z}}\bar{T}^N(\bar{z},t)\bar{\varphi}_k^N(\bar{z})\big]_0^1$$
$$- \langle \partial_{\bar{z}}\bar{T}^N(\bar{z},t)|\partial_{\bar{z}}\bar{\varphi}_k^N(\bar{z})\rangle \Big) \quad (16)$$
$$+ \langle a_1(\bar{z},t)\partial_{\bar{z}}\bar{T}^N(\bar{z},t)|\bar{\varphi}_k^N(\bar{z})\rangle + \langle \bar{\boldsymbol{\psi}}(\bar{z},t)|\bar{\varphi}_k^N(\bar{z})\rangle \bar{\boldsymbol{u}}_{\mathrm{m}}(t).$$

Finally, by utilising the boundary conditions (11b), (11c) and substituting the test solution (14) the system can be written in matrix-vector notation:

$$\dot{\boldsymbol{w}}^N(t) = -a_2(t)\Big(\boldsymbol{P}_2\bar{\boldsymbol{w}}^N(t) + \boldsymbol{q}_2 T_{\mathrm{m}} + \boldsymbol{q}_0\bar{u}(t)\Big)$$
$$+ \frac{\dot{\gamma}(t)}{\beta(t)}\big(\boldsymbol{P}_1\bar{\boldsymbol{w}}^N(t) + \boldsymbol{q}_1 T_{\mathrm{m}}\big) \quad (17)$$
$$- \frac{\bar{u}_{\mathrm{v}}(t)}{\beta(t)}\big(\boldsymbol{P}_3\bar{\boldsymbol{w}}^N(t) + \boldsymbol{q}_3 T_{\mathrm{m}}\big) + \boldsymbol{\Xi}\boldsymbol{\Theta}(t)\bar{\boldsymbol{u}}_{\mathrm{m}}(t)$$

with the matrices $\boldsymbol{P}_i$, $\boldsymbol{\Xi}$ and $\boldsymbol{\Theta}(t)$ as well as the vectors $\boldsymbol{q}_i$ given in Appendix B. Thus, ordinary differential equation systems (ODESs) for the weights of the solid and liquid phase – given by $\bar{\boldsymbol{w}}_{\mathrm{s}}^N(t)$ and $\bar{\boldsymbol{w}}_{\mathrm{l}}^N(t)$, respectively – are obtained. Finally, writing (11d) in the new variables yields:

$$\dot{\gamma}(t) = \partial_{\bar{z}}\bar{\boldsymbol{\varphi}}^N(1)\Big(s_{\mathrm{s}}(t)\bar{\boldsymbol{w}}_{\mathrm{s}}^N(t) + s_{\mathrm{l}}(t)\bar{\boldsymbol{w}}_{\mathrm{l}}^N(t)\Big)$$
$$+ \partial_{\bar{z}}\bar{\varphi}_N^N(1)T_{\mathrm{m}}\Big(s_{\mathrm{s}}(t) + s_{\mathrm{l}}(t)\Big). \quad (18)$$

3.3 State space formulation

In order to make the derived system compatible with the general state space formulation (8), firstly, the state vector

$$\boldsymbol{x}^N(t) := \Big(\big(\bar{\boldsymbol{w}}_{\mathrm{s}}^N(t)\big)^T \ \big(\bar{\boldsymbol{w}}_{\mathrm{l}}^N(t)\big)^T \ \gamma(t)\Big)^T \in \mathbb{R}^M \quad (19)$$

with dimension $M := 2(N-1)+1$, containing the temperature weights of crystal and melt as well as the interface position, is introduced. Regarding the initial state $\boldsymbol{x}^N(0)$, the initial weights for the solid or liquid phase $\bar{w}_i^N(0)$ are obtained by the projection

$$\bar{w}_i^N(0) = \langle \bar{\varphi}_i^N(\bar{z})|\bar{T}(\bar{z},0)\rangle, \quad i = 1, \ldots, N-1 \quad (20)$$

of the respective initial temperature profile onto the shape functions $\bar{\varphi}_i^N(\bar{z})$. Finally, the system input is given by

$$\boldsymbol{u}(t) := \big(\bar{u}_{\mathrm{s}}(t) \ \bar{u}_{\mathrm{m},1}(t) \ \bar{u}_{\mathrm{m},2}(t) \ \bar{u}_{\mathrm{m},3}(t) \ \bar{u}_{\mathrm{l}}(t) \ \bar{u}_{\mathrm{v}}(t)\big)^T \quad (21)$$

including the top, jacket and bottom heaters as well as the melt convection. Thus, by using the solid and liquid variant of (17) as well as (18), the approximated form reads:

$$\dot{\boldsymbol{x}}^N(t) = f^N\big(\boldsymbol{x}^N(t), \boldsymbol{u}(t)\big). \quad (22)$$

Since only approximations of the same order will be used in the following sections, the order N will be omitted where the context is clear.

4. NONLINEAR MODEL PREDICTIVE CONTROL

4.1 Constraints & costs

To comply with the modelling assumptions, a set of constraints has to be formulated for the model to remain physically plausible. In detail, for the weights $\bar{\boldsymbol{w}}_{\mathrm{s}}^N(t)$ in the crystal it is necessary to keep the temperatures below the melting temperature T_{m} while the weights $\bar{\boldsymbol{w}}_{\mathrm{l}}^N(t)$ in the melt must stay above. Similarly, to limit the expansion-induced shear stress in the crystal, a lower bound for the solid weights is needed while an upper bound for the weights in the liquid domain saves the melt from overheating. These requirements are met by enforcing $w_{\mathrm{L}} \leq \bar{w}_i^N(t) \leq w_{\mathrm{U}}$ for each phase with the respective lower and upper bounds. Furthermore, due to the limited physical extent of the system the condition $\Gamma_{\mathrm{s}} < \gamma(t) < \Gamma_{\mathrm{l}}$ must be met, yielding the state constraint vectors $\boldsymbol{x}_{\mathrm{L}}^T := \big(\boldsymbol{w}_{\mathrm{L,s}}^T \ \boldsymbol{w}_{\mathrm{L,l}}^T \ \Gamma_{\mathrm{s}}\big)$ as well as $\boldsymbol{x}_{\mathrm{U}}^T := \big(\boldsymbol{w}_{\mathrm{U,s}}^T \ \boldsymbol{w}_{\mathrm{U,l}}^T \ \Gamma_{\mathrm{l}}\big)$. Regarding the inputs, the heat flows applied by the heaters around the crucible and their time derivatives are limited. This fact is expressed via $\boldsymbol{u}_{\mathrm{L}} \leq \boldsymbol{u}(t) \leq \boldsymbol{u}_{\mathrm{U}}$ and $\boldsymbol{\nu}_{\mathrm{L}} \leq \dot{\boldsymbol{u}}(t) \leq \boldsymbol{\nu}_{\mathrm{U}}$ in which the components of the constraint vectors adhere to the ordering in (21). For the concrete values of all constraints please refer to Table D.2.

Regarding the main objective of growing a crystal, the base costs are chosen as the quadratic form

$$l_0(\boldsymbol{x}(t), \boldsymbol{u}(t)) := \tilde{\boldsymbol{x}}(t)^T \boldsymbol{Q}\tilde{\boldsymbol{x}}(t) + \boldsymbol{u}(t)^T \boldsymbol{R}\boldsymbol{u}(t) \quad (23)$$

where $\tilde{\boldsymbol{x}}(t) := \boldsymbol{x}(t) - \boldsymbol{x}_{\mathrm{ref}}$ denotes the deviation from the reference state $\boldsymbol{x}_{\mathrm{ref}}^T := \big(\bar{\boldsymbol{w}}_{\mathrm{s,ref}}(t)^T \ \bar{\boldsymbol{w}}_{\mathrm{l,ref}}(t)^T \ \gamma_{\mathrm{ref}}\big)$[2] and $\boldsymbol{Q}$ as well as $\boldsymbol{R}$ denote the weight matrices.

However, in order to obtain a high quality crystal additional process targets must be met. To avoid dislocations in the crystal lattice, the growth velocity must stay positive but below a certain level $\dot{\gamma}_{\max}$. In addition, the temperature gradient on the liquid side of the phase boundary $g_{\mathrm{l}}(t) := \partial_z T_{\mathrm{l}}^N(\gamma(t), t)$ must stay above $g_{\mathrm{l,min}}$ to prevent spontaneous crystallisation in the melt and the formation of twins. Furthermore, in reality, if the growth rate is too high and the latent heat cannot be transported away from the centre fast enough, the interface will develop a concave shape. This has to be avoided because it will lead to an unusable crystal. However, as the interface deflection cannot be accounted for in the employed one-dimensional model, the ratio of growth rate and the gradient on the solid side of the interface $\eta(t) := \dot{\gamma}(t)/\partial_z T_{\mathrm{s}}(\gamma(t), t)$ (Vanhellemont, 2013) is used instead and must stay below $\eta_{\max}$. Finally, as the objectives are formulated in the original distributed temperature $T(z, t)$ but only the approximated state $\boldsymbol{x}(t)$ is available at runtime, their approximations are derived by the means of (12), yielding $\bar{g}_{\mathrm{l}}(\boldsymbol{x}(t))$ and $\bar{\eta}(\boldsymbol{x}(t))$, respectively.

Next, instead of explicitly enforcing these process targets using constraints, they are accounted for with the terms:

$$l_1(\boldsymbol{x}(t)) := 2 + \mathrm{erf}\Big(-m_1\big(\dot{\gamma}(t) - \dot{\gamma}_{\min}\big) + o\Big)$$
$$+ \mathrm{erf}\Big(m_1\big(\dot{\gamma}(t) - \dot{\gamma}_{\max}\big) - o\Big) \quad (24)$$

---

[2] In detail, the used reference state is given as an equilibrium profile, computed for a constant growth rate $\dot{\gamma}_{\mathrm{ref}}$ and a desired solid gradient $g_{\mathrm{s,ref}} := \partial_z T_{\mathrm{s,ref}}(\gamma(t))$.

$$l_2(\boldsymbol{x}(t)) := 1 + \mathrm{erf}\Big(-m_2\big(\bar{g}_{\mathrm{l}}(\boldsymbol{x}(t)) - g_{\mathrm{l,min}}\big) + o\Big) \quad (25)$$

$$l_3(\boldsymbol{x}(t)) := 1 + \mathrm{erf}\Big(m_3\big(\bar{\eta}(\boldsymbol{x}(t)) - \eta_{\mathrm{max}}\big) - o\Big). \quad (26)$$

Herein, $\mathrm{erf}(x) := \frac{2}{\sqrt{\pi}} \int_0^x e^{-\tau^2} d\tau$ is the error function, with argument shift o and scalings m_i.

Finally, taking the weighted sum of (23) to (26), the stage cost function

$$l(\boldsymbol{x}, \boldsymbol{u}) := l_0(\boldsymbol{x}, \boldsymbol{u}) + p\big(l_1(\boldsymbol{x}(t)) + l_2(\boldsymbol{x}(t)) + l_3(\boldsymbol{x}(t))\big) \quad (27)$$

with the weighting factor p between primary and secondary objectives is obtained. All objective parameters can be found in Table D.3.

4.2 Problem statement

The spatially discretised nonlinear state space system (8) obtained in Section 3 is continuous in time and therefore needs to be reformulated as the discrete-time system

$$\boldsymbol{x}_{n+1} = \boldsymbol{f}_{\mathrm{d}}(\boldsymbol{x}_n, \boldsymbol{u}_n) \quad (28)$$

where $\boldsymbol{x}_n = \boldsymbol{x}(n\Delta t)$ with discretisation step $n \in \mathbb{N}$ and sampling time $\Delta t \in \mathbb{R}^+$ in order to apply NMPC. Both is done with the help of `MPCTools` (Risbeck M.J., 2015), an interface for the `CasADi` framework (Andersson et al., 2019). Specifically, the time discretisation is carried out using fourth-order orthogonal collocation. With this in mind, the optimal control problem to be consecutively solved on a horizon $H \in \mathbb{N}_{>1}$ can be stated as finding the optimal control

$$\boldsymbol{U}_H^* = \arg\min_{\boldsymbol{U}_H} \sum_{n=0}^{H-1} l_{\mathrm{d}}(\boldsymbol{x}_u(n, \boldsymbol{x}_0), \boldsymbol{u}_n) \quad (29a)$$

subject to

$$\boldsymbol{x}_u(0, \boldsymbol{x}_0) = \boldsymbol{x}_0 \quad (29b)$$
$$\boldsymbol{x}_u(n+1, \boldsymbol{x}_0) = \boldsymbol{f}_{\mathrm{d}}(\boldsymbol{x}_u(n, \boldsymbol{x}_0), \boldsymbol{u}_n) \quad (29c)$$
$$\boldsymbol{x}_{\mathrm{L}} \leq \boldsymbol{x}_u(n, \boldsymbol{x}_0) \leq \boldsymbol{x}_{\mathrm{U}} \quad (29d)$$
$$\boldsymbol{u}_{\mathrm{L}} \leq \boldsymbol{u}_n \leq \boldsymbol{u}_{\mathrm{U}} \quad (29e)$$
$$\boldsymbol{\nu}_{\mathrm{L}} \leq (\boldsymbol{u}_{n+1} - \boldsymbol{u}_n)/\Delta t \leq \boldsymbol{\nu}_{\mathrm{U}} \quad (29f)$$

$\forall n \in [0, H) \subset \mathbb{N}_0$ where $\boldsymbol{x}_u(n, \boldsymbol{x}_0)$ denotes the predicted system trajectory that results from applying the input sequence $\boldsymbol{U}_H := \{\boldsymbol{u}_0, \boldsymbol{u}_1, ..., \boldsymbol{u}_{H-1}\}$ starting from $\boldsymbol{x}_0$. This input sequence is to be optimized by minimizing the sum of the discrete scalar stage cost $l_{\mathrm{d}}(\boldsymbol{x}_u(n, \boldsymbol{x}_0), \boldsymbol{u}_n)$ obtained from the continuous stage cost (27) via quadrature. Since there are no equality constraints or costs associated with the terminal state $\boldsymbol{x}_H$, this particular NMPC approach can be referred to as one without stabilizing terminal conditions (cf. Grüne and Pannek, 2017).

5. RESULTS

The control design of the previous section will now be evaluated for different scenarios. To do so the FEM approximation from Section 3 will serve as a reference model for the control design, after its convergence has been discussed. Next, the control performance for an ideal case and two more realistic cases will be presented. The corresponding parameters are given in Table D.1.
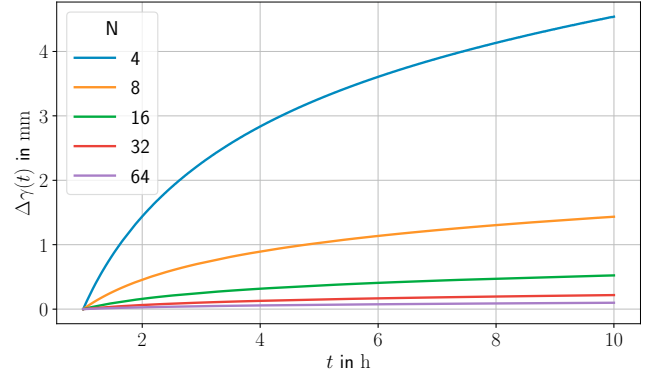

Fig. 3. Deviation of the phase boundary $\Delta\gamma(t) = \gamma^N(t) - \gamma_{\mathrm{r}}(t)$ between the simulated trajectories of the phase boundary and the analytic reference solution $\gamma_{\mathrm{r}}(t)$ in original coordinates for different approximation orders.

5.1 Model verification

To verify the convergence of the approximated model (22), a benchmark scenario (cf. Appendix C) is simulated, for which an analytic expression – the Neumann solution – exists. For the simulations, the approximation order N of the series expansion (9) is iteratively increased, yielding an approximation error that is supposed to decrease. As Figure 3 shows, the errors for $\gamma(t)$ decay for growing N as the heat transport effects can be described better by the model. For $N \geq 10$, the error falls below $1\,\mathrm{mm}$ and is below $100\,\mu\mathrm{m}$ for $N = 64$.

5.2 Control setup & implementation

For the remaining simulations, the following scenario is assumed: Initially, the phase boundary is resting ($\dot{\gamma}(0) = 0\,\mathrm{m\,s^{-1}}$) at $\gamma(0) = 0.02\,\mathrm{m}$. Furthermore, as a result of the previous melting step a gradient of $\partial_z T_{\mathrm{s}}(\gamma(0), 0) = 10\,\mathrm{K\,cm^{-1}}$ has been established throughout the crystal. Now, the control objective is to grow a valid crystal within $t_f = 70\,\mathrm{h}$. Thus, $\gamma(t)$ has to be transferred to $0.38\,\mathrm{m}$ while adhering to the objectives for the growth speed $\dot{\gamma}(t)$, the interface gradient on the liquid side $\partial_z T(\gamma(t), t)$, and the ratio $\eta(t)$.

Making a trade-off between accuracy and problem size, a model with $N_{\mathrm{cont}} = 10$ nodes per domain is used for the control design. Furthermore, a horizon length $H = 20$ with a discretisation step of $\Delta t = 30\,\mathrm{min}$ is chosen, yielding a planning domain of $\frac{1}{7}t_f = 10\,\mathrm{h}$ and a final problem with 2140 variables to be solved by `IPOPT` (Wächter and Biegler, 2006).

5.3 Reference scenario

As a baseline, a setup is chosen where the design model used by the controller exactly matches the simulated system which will be referred to as scenario A. Figure 4 shows that in this case, a crystal of the desired length can be grown within the given time frame. As can be seen from the associated control inputs in Figure 6, the controller primarily exploits the bottom heater for this purpose. Finally, Figure 7 shows that all secondary objectives are fulfilled with an initial exception for the liquid gradient.
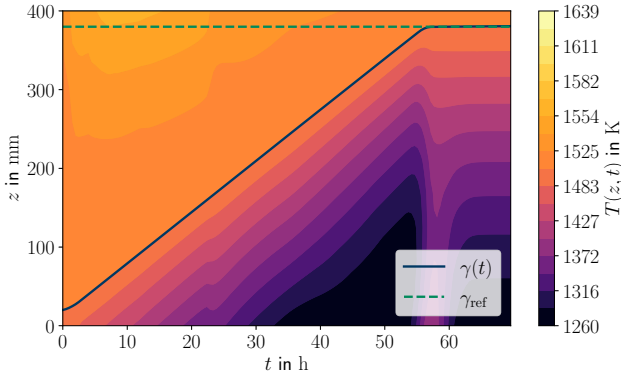
Fig. 4. Resulting temperature profile $T(z,t)$ with the corresponding phase boundary $\gamma(t)$ (blue, solid) and its reference (green, dashed) for simulation case A.

5.4 Model errors

In reality, the design model used for the controller differs from the plant. Hence, in order to investigate the influence of model errors on the controller performance, an approximation order $N_{\text{sim}} = 64$ is used for the simulation model in scenario B while the controller model stays at $N_{\text{cont}} = 10$. In this case the crystal also manages to reach its desired length but the input trajectories in Figure 6 show that the controller is struggling and relying more on the lower and middle jacket heater. However, this time the gradient objective in Figure 7 is violated at 27 h.

Finally, the performance in the presence of parameter uncertainties is investigated. For this purpose the physical simulation parameters from the previous scenario were altered to reflect a relative error of 10 % (cf. lower part of Table D.1). This is referred to as scenario C. As can be seen in Figure 5, the controller has to increase the melt temperature within the growth process. Furthermore, the input trajectories in Figure 6 changed drastically with the most significant difference being the maximum usage of the top heater. Lastly, Figure 7 shows that the objectives can still be mostly satisfied, with the apparent exception of the liquid gradient falling below the desired minimum between 10 h and 30 h. This issue arises from the fact that the controller fails to lower the solid gradient and thus makes a trade-off to reach a feasible growth velocity by means of (7).

6. CONCLUSION AND OUTLOOK

In this contribution, a NMPC design has been presented for a two-phase Stefan problem, occurring in the VGF process. By utilising not only the heat flows but also the forced melt convection as control inputs, this approach is able to keep up with most process requirements, even under the influence of modelling errors and parameter uncertainties.

The next obvious step is to evaluate the control against a two-dimensional plant model that is able to represent a curved crystallisation interface which is the minimum requirement for a real-life application. However, effects like introduced dislocations due to temperature-induced stress in the crystal (Jordan et al., 1984) or occurrence of impurities and their rejection occurring at the solid-liquid interface
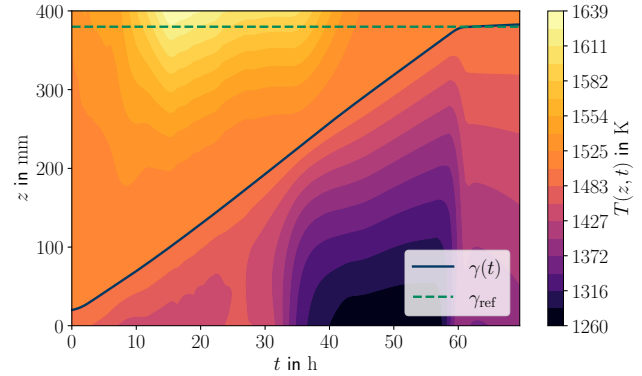

Fig. 5. Resulting temperature profile $T(z,t)$ with the corresponding phase boundary $\gamma(t)$ (blue, solid) and its reference (green, dashed) for simulation case C.
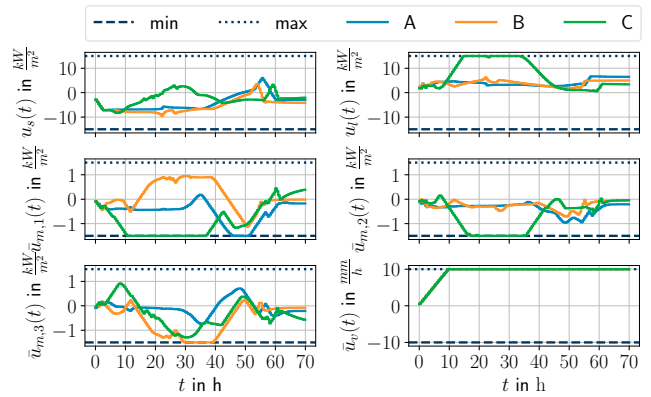
Fig. 6. Input trajectories with respective boundaries for ideal (A), real (B) and erroneous case (C).
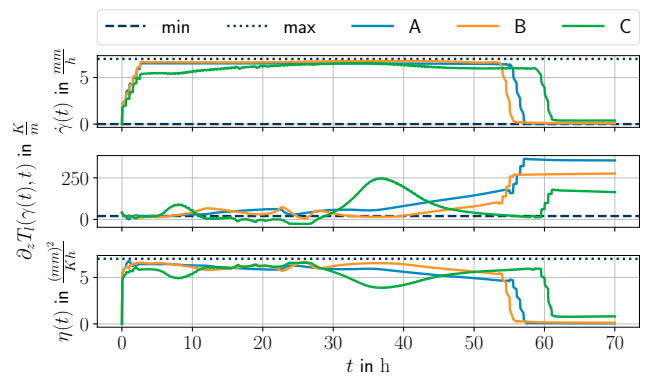
Fig. 7. Process objective trajectories with desired minima and maxima (cf. Table D.3) for the ideal (A), real (B) and erroneous case (C).

in the crystallisation process (Zhu et al., 2006; Duseaux, 1983) are key elements to improve crystal quality. Therefore, directly modelling these effects instead of keeping them in check indirectly via gradient ratios represents another possible step to improve the applicability. On the other hand, the presented one-dimensional approximation could be substituted by an artificial neural network (ANN) for which first results (Dropka et al., 2021) look promising, although

impurities are not yet considered. These issues are currently under investigation by the authors. The source code of this contribution is available under `https://gitlab.hrz.tu-chemnitz.de/tud-rst/publications/2021-nmpc`.

REFERENCES

Abdollahi, J., Izadi, M., and Dubljevic, S. (2014). Model predictive temperature tracking in crystal growth processes. *Computers & Chemical Engineering*, 71, 323 – 330. doi:10.1016/j.compchemeng.2014.09.005.

Alexiades, V. and Solomon, A.D. (1993). *Mathematical Modeling of Melting or Freezing Processes*. Taylor & Francis, first edition. doi:10.1201/9780203749449.

Andersson, J.A.E., Gillis, J., Horn, G., Rawlings, J.B., and Diehl, M. (2019). CasADi – A software framework for nonlinear optimization and optimal control. *Mathematical Programming Computation*, 11(1), 1–36. doi:10.1007/s12532-018-0139-4.

Crank, J. (1984). *Free and Moving Boundary Problems (Oxford Science Publications)*. Oxford Science Publications. Oxford University Press.

Dropka, N., Ecklebe, S., and Holena, M. (2021). Real Time Predictions of VGF-GaAs Growth Dynamics by LSTM Neural Networks. *Crystals*, 11(2). doi:10.3390/cryst11020138.

Duseaux, M. (1983). Temperature profile and thermal stress calculations in GaAs crystals growing from the melt. *Journal of Crystal Growth*, 61(3), 576–590. doi:10.1016/0022-0248(83)90186-0.

Ecklebe, S., Woittennek, F., Frank-Rotsch, C., Dropka, N., and Winkler, J. (2021). Toward Model-Based Control of the Vertical Gradient Freeze Crystal Growth Process. *IEEE Transactions on Control Systems Technology*, 1–8. doi:10.1109/TCST.2021.3058006.

Ecklebe, S., Woittennek, F., and Winkler, J. (2020). Control of the vertical Gradient Freeze crystal growth process via backstepping. *IFAC-PapersOnLine*, 53(2), 7758–7764. doi:10.1016/j.ifacol.2020.12.1537. 21th IFAC World Congress.

Frank-Rotsch, C., Dropka, N., Glacki, A., and Juda, U. (2014). VGF growth of GaAs utilizing heater-magnet module. *Journal of Crystal Growth*, 401, 702–707.

Friedrich, J., von Ammon, W., and Müller, G. (2015). 2 - czochralski growth of silicon crystals. In P. Rudolph (ed.), *Handbook of Crystal Growth*, 45 – 104. Elsevier, Boston, second edition. doi:10.1016/B978-0-444-63303-3.00002-X.

Grüne, L. and Pannek, J. (2017). *Nonlinear Model Predictive Control*. Springer, Cham, 2 edition. doi:10.1007/978-3-319-46024-6.

Hinze, M., Pätzold, O., and Ziegenbalg, S. (2009). Solidification of a GaAs melt—Optimal control of the phase interface. *Journal of Crystal Growth*, 311(8), 2501 – 2507. doi:10.1016/j.jcrysgro.2009.02.031.

Jordan, A., von Neida, A., and Caruso, R. (1984). The theory and practice of dislocation reduction in GaAs and InP. *Journal of Crystal Growth*, 70(1), 555–573. doi:x10.1016/0022-0248(84)90318-X.

Jurisch, M., Börner, F., Bünger, T., Eichler, S., Flade, T., Kretzer, U., Köhler, A., Stenzenberger, J., and Weinert, B. (2005). LEC- and VGF-growth of SI GaAs single crystals—recent developments and current issues.

Journal of Crystal Growth, 275(1), 283 – 291. doi:10.1016/j.jcrysgro.2004.10.092.

Kang, S. and Zabaras, N. (1995). Control of the freezing interface motion in two-dimensional solidification processes using the adjoint method. *International Journal for Numerical Methods in Engineering*, 38(1), 63–80. doi:10.1002/nme.1620380105.

Koga, S., Diagne, M., and Krstic, M. (2019). Control and State Estimation of the One-Phase Stefan Problem via Backstepping Design. *IEEE Transactions on Automatic Control*, 64(2), 510–525. doi:10.1109/TAC.2018.2836018.

Maidi, A. and Corriou, J.P. (2014). Boundary geometric control of a linear Stefan problem. *Journal of Process Control*, 24(6), 939 – 946. doi:10.1016/j.jprocont.2014.04.010. Energy Efficient Buildings Special Issue.

Petrus, B., Bentsman, J., and Thomas, B.G. (2010). Feedback control of the two-phase Stefan problem, with an application to the continuous casting of steel. In *49th IEEE Conference on Decision and Control (CDC)*, 1731–1736. doi:10.1109/CDC.2010.5717456.

Rahmanpour, P., Sælid, S., Hovd, M., Grønning, O., and Jomaa, M. (2016). Nonlinear model predictive control of the czochralski process. *IFAC-PapersOnLine*, 49(20), 120 – 125. doi:10.1016/j.ifacol.2016.10.107. 17th IFAC Symposium on Control, Optimization and Automation in Mining, Mineral and Metal Processing MMM 2016.

Risbeck M.J., R.J. (2015). MPCTools: Nonlinear model predictive control tools for CasADi (Python interface). URL `https://bitbucket.org/rawlings-group/mpc-tools-casadi`.

Stefan, J. (1891). Über die Theorie der Eisbildung, insbesondere über die Eisbildung im Polarmeere. *Annalen der Physik*, 278(2), 269–286. doi:10.1002/andp.18912780206.

Vanhellemont, J. (2013). The v/g criterion for defect-free silicon single crystal growth from a melt revisited: Implications for large diameter crystals. *Journal of Crystal Growth*, 381, 134 – 138. doi:10.1016/j.jcrysgro.2013.06.039.

Wouwer, A.V., Saucez, P., and Schiesser, W. (2001). *Adaptive method of lines*. Chapman & Hall/CRC Press, first edition.

Wächter, A. and Biegler, L.T. (2006). On the implementation of an interior-point filter line-search algorithm for large-scale nonlinear programming. *Mathematical Programming*, 106(1), 25–57. doi:10.1007/s10107-004-0559-y.

Zhu, X., Sheu, G., and Tsai, C. (2006). Finite element modeling of dislocation reduction in GaAs and InP single crystals grown from the VGF process. *Finite Elements in Analysis and Design*, 43(1), 81–92. doi:10.1016/j.finel.2006.07.003.

Appendix A. BOUNDARY IMMOBILISATION METHOD

To express the system in the fixed coordinates (10), the partial derivatives with respect to t and z

$$\partial_t T(z,t) = \partial_t \left(\bar{T}(\bar{z},t) \right) = \partial_{\bar{z}}\bar{T}(\bar{z},t)\partial_t\bar{z} + \partial_t\bar{T}(\bar{z},t)$$

$$= -\frac{\bar{z}\dot{\gamma}(t)}{\beta(t)}\partial_{\bar{z}}\bar{T}(\bar{z},t) + \partial_t\bar{T}(\bar{z},t) \tag{A.1a}$$

$$\partial_z T(z,t) = \partial_{\bar{z}} \bar{T}(\bar{z},t)\partial_z \bar{z} = \frac{1}{\beta(t)}\partial_{\bar{z}}\bar{T}(\bar{z},t) \qquad \text{(A.1b)}$$

$$\partial_z^2 T(z,t) = \frac{1}{\beta^2(t)}\partial_{\bar{z}}^2 \bar{T}(\bar{z},t) \qquad \text{(A.1c)}$$

are taken. Reassembling (6) with (A.1a), (A.1b) and (A.1c), one arrives at the transformed system

$$\partial_t \bar{T}(\bar{z},t) = a_2(t)\partial_{\bar{z}}^2 \bar{T}(\bar{z},t) + a_1(\bar{z},t)\partial_{\bar{z}}\bar{T}(\bar{z},t) + \bar{\psi}(\bar{z},t)\bar{u}_{\mathrm{m}}(t)$$
$$\partial_{\bar{z}}\bar{T}(0,t) = \bar{u}(t)$$
$$\bar{T}(1,t) = T_{\mathrm{m}}$$

with $a_2(t) := \alpha/\beta^2(t)$, $a_1(\bar{z},t) := (\bar{z}\dot{\gamma}(t) - \bar{\psi}_{\mathrm{v}}(\bar{z})\bar{u}_{\mathrm{v}}(t))/\beta(t)$, $\bar{\psi}_{\mathrm{v}}(\bar{z}) := \psi_{\mathrm{v}}(z)$, $\bar{q}_{\mathrm{m}}(\bar{z},t) := q_{\mathrm{m}}(z,t)$, and $\bar{u}(t) := \frac{\delta}{\lambda}\beta(t)u(t)$. Finally, inserting (A.1b) into (7) for both phases yields

$$\dot{\gamma}(t) = s_{\mathrm{s}}(t)\partial_{\bar{z}}\bar{T}_{\mathrm{s}}(1,t) + s_{\mathrm{l}}(t)\partial_{\bar{z}}\bar{T}_{\mathrm{l}}(1,t)$$

with $s(t) := -\delta\lambda/(L\rho_{\mathrm{m}}\beta(t))$.

Appendix B. MATRICES, VECTORS AND PARAMETERS

Let a matrix $\boldsymbol{A} \in \mathbb{R}^{m\times n}$ be given by its elements $\boldsymbol{A} := [a_{ki}]$ for $k = 1,\ldots,m$ and $i = 1,\ldots,n$. Thus, computing each scalar product in (16) for every $\bar{\varphi}_i^N(\bar{z})$ in (14) and $\bar{\varphi}_k^N(\bar{z})$ in $\bar{\boldsymbol{\varphi}}^N(\bar{z})$ yields the objects

$$\boldsymbol{P}_0 := \left[\langle \bar{\varphi}_i^N(\bar{z})|\bar{\varphi}_k^N(\bar{z})\rangle\right],\ \boldsymbol{P}_1 := \boldsymbol{P}_0^{-1}\left[\langle \bar{z}\partial_{\bar{z}}\bar{\varphi}_i^N(\bar{z})|\bar{\varphi}_k^N(\bar{z})\rangle\right]$$
$$\boldsymbol{P}_2 := \boldsymbol{P}_0^{-1}\left[\langle \partial_{\bar{z}}\bar{\varphi}_i^N(\bar{z})|\partial_{\bar{z}}\bar{\varphi}_k^N(\bar{z})\rangle\right]$$
$$\boldsymbol{P}_3 := \boldsymbol{P}_0^{-1}\left[\langle \bar{\psi}_{\mathrm{v}}(\bar{z})\partial_{\bar{z}}\bar{\varphi}_i^N(\bar{z})|\bar{\varphi}_k^N(\bar{z})\rangle\right]$$
$$\boldsymbol{q}_0 := \boldsymbol{P}_0^{-1}\bar{\boldsymbol{\varphi}}^N(0),\ \boldsymbol{q}_1 := \boldsymbol{P}_0^{-1}\left[\langle \bar{z}\partial_{\bar{z}}\bar{\varphi}_N^N(\bar{z})|\bar{\varphi}_k^N(\bar{z})\rangle\right]$$
$$\boldsymbol{q}_2 := \boldsymbol{P}_0^{-1}\left[\langle \partial_{\bar{z}}\bar{\varphi}_N^N(\bar{z})|\partial_{\bar{z}}\bar{\varphi}_k^N(\bar{z})\rangle\right]$$
$$\boldsymbol{q}_3 := \boldsymbol{P}_0^{-1}\left[\langle \bar{\psi}_{\mathrm{v}}(\bar{z})\partial_{\bar{z}}\bar{\varphi}_N^N(\bar{z})|\bar{\varphi}_k^N(\bar{z})\rangle\right]$$

for $1 \le k, i \le N - 1$. Furthermore, by using the separation $\bar{\psi}(\bar{z},t) = \bar{\boldsymbol{\rho}}(\bar{z})\boldsymbol{\Theta}(t)$ with $\bar{\boldsymbol{\rho}}(\bar{z}) = (1, \bar{z}, \bar{z}^2)$ and $\boldsymbol{\Theta}(t) = \left[\theta_j^T(t)\right]$ where $\theta_j(t) = (b_i\Gamma^2 + c_i\Gamma + d_i,\ \beta(t)(2b_i\Gamma + c_i),\ b_i\beta^2(t))$ for with $1 \le j \le 3$, the vector $\boldsymbol{\Xi} := \boldsymbol{P}_0^{-1}\left[\langle \bar{\rho}_j(\bar{z})|\bar{\varphi}_k^N(\bar{z})\rangle\right]$ can be computed.

Appendix C. VERIFICATION SETUP

To get a benchmark for the approximated system, the solution for a special case is considered. Herein, a semi-infinite stripe of liquid with constant initial temperature $T(z,0) = T_{\mathrm{m}} + 100\,\mathrm{K}$ is assumed, which gets solidified by prescribing the temperature on one side to be $T(0,t) = T_{\mathrm{m}} - 100\,\mathrm{K}$ for $t > 0$. It is further assumed that the materials density ρ is constant for the crystalline and liquid domain and matches ρ_{m} from Table D.1, therefore possessing the thermal diffusivities $\tilde{\alpha}_s = 2.964 \times 10^{-6}$ and $\tilde{\alpha}_l = 7.179 \times 10^{-6}$. For this scenario, e.g. (Alexiades and Solomon, 1993) offers an analytic solution for the evolution of the phase boundary, taking the form of a root function. However, as each domain must be of a length greater zero for the immobilised transform (10) to be well defined, the initial state for the numeric simulation is sampled from the analytic solution at $t = 1\,\mathrm{h}$. Finally, by evaluating the analytic temperature profile at the boundaries, the required heat flows for the simulation can be computed such that the semi-infinite system is mapped to a finite system with a homogeneous Neumann boundary on the liquid side.

Appendix D. PARAMETERS

Table D.1. Control and simulation parameters

Name	Symbol	Value (s/l)	Unit
Sp. ht. cap. (cont)	c_{p}	423.59 / 434	J/(kgK)
Th. cond. (cont)	k	7.17 / 17.80	W/(mK)
Th. diffus. (cont)	α_{s}	$3.27 \times 10^{-6}/$	$\mathrm{m^2\,s^{-1}}$
	α_{l}	7.19×10^{-6}	$\mathrm{m^2\,s^{-1}}$
Densities (cont)	ρ_{s}	5171.24 /	$\mathrm{kg\,m^{-3}}$
	ρ_{l}	5702.37	$\mathrm{kg\,m^{-3}}$
	ρ_{m}	5713.07	$\mathrm{kg\,m^{-3}}$
Melting temp.	T_{m}	1511.15	K
Sp. lt. heat (cont)	L	6.685×10^5	$\mathrm{J\,kg^{-1}}$
Boundaries	$\Gamma_{\mathrm{s}}, \Gamma_{\mathrm{l}}$	0, 0.4	m
Geometric	b_1, b_2, b_3	-14.06	
factors of $\psi_i(z)$	c_1, c_2, c_3	3.75, 5.63, 7.5	
	d_1, d_2, d_3	0.75, 0.44, 0	
Av. Vort. Char.	$\bar{\psi}_{\mathrm{v}}(\bar{z}) = 1$		
Nodes (cont)	N_{cont}	10	
Sp. ht. cap. (sim)	c_{p}'	465.95 / 477.4	J/(kgK)
Th. cond. (sim)	k'	7.89 / 19.48	W/(mK)
Th. diffus. (sim)	α_{s}'	$2.977 \times 10^{-6}/$	$\mathrm{m^2\,s^{-1}}$
	α_{l}'	6.539×10^{-6}	$\mathrm{m^2\,s^{-1}}$
Densities (sim)	ρ_{s}'	5688.32 /	$\mathrm{kg\,m^{-3}}$
	ρ_{l}'	6272.64	$\mathrm{kg\,m^{-3}}$
	ρ_{m}'	6284.41	$\mathrm{kg\,m^{-3}}$
Sp. lt. heat (sim)	L'	7.3535×10^5	$\mathrm{J\,kg^{-1}}$
Nodes (sim)	N_{sim}	41	

Table D.2. System constraints

Variable	Symbol	Bounds		Unit
	$\square$	$\square_{\mathrm{L}}$	$\square_{\mathrm{U}}$	
Temperatures	$\bar{w}_{\mathrm{s}}^N$	1300	1511	K
	$\bar{w}_{\mathrm{l}}^N$	1512	1800	K
Heat flows	$\bar{u}_{\mathrm{s}}, \bar{u}_{\mathrm{l}}$	-15	15	$\mathrm{kW\,m^{-2}}$
	$\bar{u}_{\mathrm{m}}$	-1.5	1.5	$\mathrm{kW\,m^{-2}}$
Heat flow der.	$\dot{u}_{\mathrm{s}}, \dot{u}_{\mathrm{l}}$	-1.8	1.8	$\mathrm{kW/(m^2h)}$
	$\dot{u}_{\mathrm{m}}$	-180	180	$\mathrm{W/(m^2h)}$
Convection	$\bar{u}_{\mathrm{v}}$	-10	10	$\mathrm{mm\,h^{-1}}$
Convection der.	$\dot{u}_{\mathrm{v}}$	-1	1	$\mathrm{mm\,h^{-1}}$

Table D.3. Growth references and objectives

Parameter	Symbol	Value	Unit
Ref. growth vel.	$\dot{\gamma}_{\mathrm{ref}}$	5	$\mathrm{mm\,h^{-1}}$
Ref. solid grad.	$g_{\mathrm{s,ref}}$	2000	$\mathrm{K\,m^{-1}}$
State weights	$\boldsymbol{Q} = \mathrm{blockdiag}(\boldsymbol{I}_d{}^*, 1e11)$		
Input weights	$\boldsymbol{R}$	$\boldsymbol{I}_6$	
Min. growth vel.	$\dot{\gamma}_{\mathrm{min}}$	0	$\mathrm{mm\,h^{-1}}$
Max. growth vel.	$\dot{\gamma}_{\mathrm{max}}$	7	$\mathrm{mm\,h^{-1}}$
Min. liq. grad.	$g_{\mathrm{l,min}}$	20	$\mathrm{K\,m^{-1}}$
Max. ratio	η_{max}	6	$\mathrm{mm^2/(Kh)}$
	m_1	3.6×10^7	
Slope factors	m_2	10	
	m_3	1×10^5	
Offset	o	2	
Rel. factor	p	1×10^{11}	

$^*\,d = 2N_{\mathrm{cont}} - 1$